The Astrophysical Journal, 877:152 (13pp), 2019 June 1 https://doi.org/10.3847/1538-4357/ab1a3f

Red and Reddened: Ultraviolet through Near-infrared Observations of Type Ia Supernova 2017erp*

Peter J. Brown[1,2], Griffin Hosseinzadeh[3], Saurabh W. Jha[4], David Sand[5], Ethan Vieira[6], Xiaofeng Wang[7], Mi Dai[4], Kyle G. Dettman[4], Jeremy Mould[8,9], Syed Uddin[10], Lifan Wang[1,2,11], Iair Arcavi[12], Joao Bento[13], Chris R. Burns[10], Tiara Diamond[14], Daichi Hiramatsu[15,16], D. Andrew Howell[15,16], E. Y. Hsiao[17], G. H. Marion[18], Curtis McCully[15,16], Peter A. Milne[5], Davron Mirzaqulov[19], Ashley J. Ruiter[8,13,20], Stefano Valenti[21], and Danfeng Xiang[7]

[1] Department of Physics and Astronomy, Texas A&M University, 4242 TAMU, College Station, TX 77843, USA; pbrown@physics.tamu.edu
[2] George P. and Cynthia Woods Mitchell Institute for Fundamental Physics & Astronomy, Texas A&M University, College Station, TX 77843, USA
[3] Center for Astrophysics | Harvard & Smithsonian, 60 Garden Street, Cambridge, MA 02138-1516, USA
[4] Department of Physics and Astronomy, Rutgers the State University of New Jersey, 136 Frelinghuysen Road, Piscataway, NJ 08854, USA
[5] Steward Observatory, University of Arizona, 933 North Cherry Avenue, Tucson, AZ 85721, USA
[6] Department of Aerospace Engineering, Texas A&M University, 4242 TAMU, College Station, TX 77843, USA
[7] Physics Department/Tsinghua Center for Astrophysics, Tsinghua University; Beijing, 100084, People's Republic of China
[8] ARC Centre of Excellence for All-Sky Astrophysics (CAASTRO), Australia
[9] Centre for Astrophysics and Supercomputing, Swinburne University of Technology, Melbourne, Victoria, Australia
[10] Observatories of the Carnegie Institution for Science, 813 Santa Barbara Street, Pasadena, CA 91101, USA
[11] Purple Mountain Observatory, Chinese Academy of Sciences, Nanjing, Jiangshu, People's Republic of China
[12] The School of Physics and Astronomy, Tel Aviv University, Tel Aviv 69978, Israel
[13] Research School of Astronomy and Astrophysics, Mount Stromlo Observatory, Australian National University, Cotter Road, Weston, Creek, ACT, 2611, Australia
[14] Goddard Space Flight Center, 8800 Greenbelt Road, Greenbelt, MD 20771, USA
[15] Las Cumbres Observatory, 6740 Cortona Drive, Suite 102, Goleta, CA, 93117-5575, USA
[16] Department of Physics, University of California, Santa Barbara, Santa Barbara, CA, 93106-9530, USA
[17] Department of Physics, Florida State University, Tallahassee, FL 32306, USA
[18] University of Texas at Austin, 1 University Station C1400, Austin, TX, 78712-0259, USA
[19] Ulugh Beg Astronomical Institute, Uzbekistan Academy of Sciences, Uzbekistan, Tashkent, 100052, Uzbekistan
[20] School of Science, University of New South Wales, Australian Defence Force Academy, Canberra, ACT 2600, Australia
[21] Department of Physics, University of California, Davis, 1 Shields Avenue, Davis, CA 95616-5270, USA
Received 2018 August 14; revised 2019 April 11; accepted 2019 April 11; published 2019 June 5

Abstract

We present space-based ultraviolet/optical photometry and spectroscopy with the *Swift* Ultra-Violet/Optical Telescope and *Hubble Space Telescope* (*HST*), respectively, along with ground-based optical photometry and spectroscopy and near-infrared spectroscopy of supernova SN 2017erp. The optical light curves and spectra are consistent with a normal SN Ia. Compared to previous photometric samples in the near-ultraviolet (NUV), SN 2017erp has UV colors that are redder than NUV-blue SNe Ia corrected to similar optical colors. The chromatic difference between SNe 2011fe and 2017erp is dominated by the intrinsic differences in the UV rather than the expected dust reddening. This chromatic difference is similar to the SALT2 color law, derived from rest-frame ultraviolet photometry of higher redshift SNe Ia. Differentiating between intrinsic UV diversity and dust reddening can have important consequences for determining cosmological distances with rest-frame ultraviolet photometry. This ultraviolet spectroscopic series is the first from *HST* of a normal, albeit reddened, NUV-red SN Ia and is important for analyzing SNe Ia with intrinsically redder NUV colors. We show model comparisons suggesting that metallicity could be the physical difference between NUV-blue and NUV-red SNe Ia, with emission peaks from reverse fluorescence near 3000 Å implying a factor of ∼10 higher metallicity in the upper layers of SN 2017erp compared to SN 2011fe. Metallicity estimates are very model dependent, however, and there are multiple effects in the UV. Further models and UV spectra of SNe Ia are needed to explore the diversity of SNe Ia, which show seemingly independent differences in the near-UV peaks and mid-UV flux levels.

Key words: dust, extinction – supernovae: general – supernovae: individual (SN2017erp, SN2011fe, SN2011by)

Supporting material: machine-readable table

1. Introduction

SNe Ia are excellent standard candles because their optical absolute magnitudes have a low dispersion, which can be further reduced using relationships between the absolute magnitude of an SN and its light-curve shape and/or colors (Phillips 1993; Riess et al. 1996; Phillips et al. 1999; Tripp & Branch 1999; Goldhaber et al. 2001; Wang et al. 2005). SNe Ia are used to constrain cosmological parameters such as Ω_M and Λ and the dark energy equation of state (e.g., Riess et al. 1998, 2004; Perlmutter et al. 1999; Betoule et al. 2014; Scolnic et al. 2018).

Despite this optical uniformity, SNe Ia have been found to be much more diverse at ultraviolet (UV) wavelengths (Ellis et al. 2008; Foley et al. 2008a; Brown et al. 2010, 2014b; Cooke et al. 2011; Wang et al. 2012; Milne et al. 2013; Brown 2014; Foley et al. 2016). In addition to a larger dispersion in the rest-frame near-UV (NUV; covering roughly 2700–4000 Å), the

* Based on observations made with the NASA/ESA *Hubble Space Telescope*, obtained at the Space Telescope Science Institute, which is operated by the Association of Universities for Research in Astronomy, Inc., under NASA contract NAS 5-26555. These observations are associated with program #14665.

SNe Ia observed in the rest-frame NUV locally are found to be systematically redder than those at redshifts $z > 0.3$ (Foley et al. 2012a; Maguire et al. 2012; Milne et al. 2015).

One of the unexpected results from the large sample of *Swift* SNe is a possible bimodal distribution of the NUV-optical colors of optically "normal" SNe Ia. Milne et al. (2013) find about one-third of SNe Ia (dubbed "NUV-blue") to have significantly bluer (by about 0.5 mag) NUV to optical colors. In this schema, the systematic shift in NUV colors with redshift is interpreted as a change in the fractions of SNe Ia whose properties are otherwise similar (Milne et al. 2015). As the majority of nearby SNe Ia belong to the NUV-red category (though the fractions depend on whether and how extinction is corrected; Brown et al. 2017), they might be considered the most "normal" SNe Ia locally. A well-studied example of an NUV-red SN Ia is the "golden standard" SN 2005cf (Wang et al. 2009b). SN 2011fe is now used as the de facto standard of normality, but it is actually among the bluest of the NUV-blue SNe (Brown et al. 2017).

UV spectroscopic comparisons have mostly focused on the NUV because of the steep drop in flux shortward of that and the limited wavelength range redshifted into the optical (Ellis et al. 2008; Foley et al. 2008a, 2008b; Bufano et al. 2009; Cooke et al. 2011; Maguire et al. 2012; Wang et al. 2012; Foley et al. 2016; Pan et al. 2018). UV photometric studies have found that the photometric scatter in peak luminosity increases at shorter wavelengths (Brown et al. 2010). With $uvm2 - uvw1$ colors of 1.2–2.5 at optical maximum, the NUV-blue SNe are generally bluer in the mid-UV (MUV; 1600–2500 Å) than the NUV-red SNe ($2.5 < uvm2 - uvw1 < 3.5$), but there is a lot of scatter and some overlap (Brown et al. 2017). The differences are strongest at early times but seem to converge at a common color about 20 days after maximum light. At early epochs the UV comes from the outermost layers of the SN ejecta, so this could probe either progenitor metallicity or the density gradient of the layers from which the UV is emitted. While the general increase in dispersion to shorter wavelengths could have a single cause, Foley & Kirshner (2013) identified two "twin" SNe Ia that have nearly identical spectra in the NUV and optical but different continuum levels in the MUV. This suggests the UV dispersion could have multiple components from different sources.

Many physical differences have strong effects in the UV (Brown et al. 2015), including metallicity (Höflich et al. 1998; Lentz et al. 2000; Sauer et al. 2008; Walker et al. 2012), asymmetry (Kasen & Plewa 2007; Kromer & Sim 2009), and density gradients (Sauer et al. 2008; Mazzali et al. 2014). Dust reddening is a strong external effect (e.g., Amanullah et al. 2014; Foley et al. 2014; Brown et al. 2015). Most of the modeling has been done with limited UV information, with the normal SN 2011fe (Mazzali et al. 2014) and the broad light curve SN 2010jn (Hachinger et al. 2013) as well-studied exceptions. The number of UV spectra has expanded greatly in the past several years (e.g., Smitka 2016 and Pan et al. 2018), especially with high-quality UV spectra from *HST* (Foley et al. 2012b; Pan et al. 2015; Foley et al. 2016). These *HST* observations now span most of the range of light-curve shapes (Foley et al. 2016) and found differences in the mid-UV for SNe similar in the NUV (Foley & Kirshner 2013), but only limited studies (Milne et al. 2015; Smitka 2016) have probed the spectral cause of the NUV differences seen in the *Swift*/UltraViolet Optical Telescope (UVOT) photometry among normal SNe Ia (Milne et al. 2013; Brown et al. 2017). Additional spectra will allow for detailed modeling similar to that done for SNe 2010jn and 2011fe (Hachinger et al. 2013; Mazzali et al. 2014).

Timmes et al. (2003) and Mazzali & Podsiadlowski (2006) showed how a change in the metallicity of the progenitor can affect the ratio of radioactive to nonradioactive Ni, and thus the luminosity and width of the light curve in a way not accounted for in the empirical relations (see also Miles et al. 2016). This could be the origin of the luminosity difference between the optical twins SNe 2011by and 2011fe (Foley & Kirshner 2013; Graham et al. 2015b; Foley et al. 2018). Metallicity differences could be responsible for the scatter in the luminosity–width relations seen locally and lead to systematic differences at high redshift due to chemical evolution of the universe as a whole and the individual star formation history in the individual galaxies and star-forming regions in which the progenitors are formed (Höflich et al. 2000; Podsiadlowski et al. 2006; Bravo et al. 2010; Moreno-Raya et al. 2016). Metallicity differences will appear strongest in the UV due to the larger line opacities (see Lentz et al. 2000; Sauer et al. 2008; Walker et al. 2012). However, the other physical differences mentioned above (e.g., density gradients, asymmetry, and explosion models) have strong effects in the UV (Brown et al. 2015, 2018). Determining whether the UV dispersion is caused by something like metallicity, which evolves with redshift, or asymmetry/viewing angle, which does not, is important to the cosmological impact of the UV dispersion.

Despite the NUV-red SNe Ia being the majority of local SNe Ia (Milne et al. 2015), the three most normal SNe Ia with high signal-to-noise ratio (S/N) UV spectroscopy from the *Hubble Space Telescope* (*HST*) are all NUV-blue SNe Ia, including the twin NUV-blue SNe 2011by and 2011fe (Foley & Kirshner 2013), and SN 2015F (Foley et al. 2016), which appears to be a reddened NUV-blue SN Ia (Brown et al. 2017). The existing NUV spectra of NUV-red SNe Ia do not have coverage below 2500 Å to see how the flux differences extend into the mid-UV. Such spectra are also necessary for understanding the extinction and k-corrections and the effect of "red-leak" optical contamination in the *Swift*/UVOT filters. This motivated an *HST* program (#14665; PI: Brown) "Ultraviolet Spectra of a Normal Standard Candle."

In this paper we present the first *HST* UV spectroscopy of a normal, albeit reddened, NUV-red SN Ia. The *HST*, *Swift*, and ground-based observations are described in Section 2. The observations are analyzed in Section 3, with physical interpretation and consequences discussed in Section 4. We summarize in Section 5.

2. Observations

2.1. Discovery and Host Galaxy

SN 2017erp was discovered by Itagaki (2017) in images taken on 2017 June 13 15:01:28 (all dates UT). It was classified by Jha et al. (2017) as an extremely young SN Ia.

The host galaxy of SN 2017erp is NGC 5861, classified as SAB(rs)c (de Vaucouleurs et al. 1991), at a redshift of 0.006174 ± 0.000003 (Theureau et al. 2005). The redshift corresponds to a distance modulus of 32.30 ± 0.26 assuming a Hubble constant of $73\,\mathrm{km\,s^{-1}\,Mpc^{-1}}$ and a random velocity uncertainty of $300\,\mathrm{km\,s^{-1}}$.

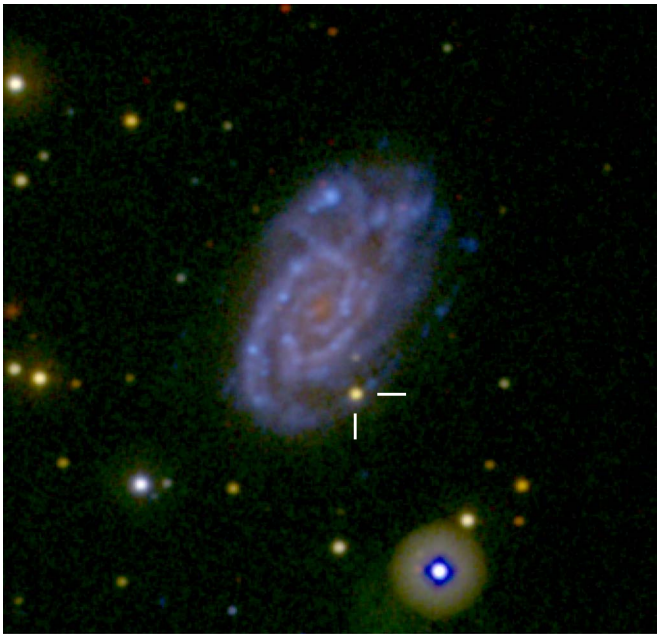

Figure 1. *Swift* UVOT color-composite image of SN 2017erp using the *uvm*2, *u*, and *v* filter images for the blue, green, and red channels respectively. The location of SN 2017erp along the faint end of a spiral arm is noted with white lines.

2.2. Swift *Photometry*

The Neil Gehrels *Swift* Observatory (Gehrels et al. 2004) began observing SN 2017erp on 2017 June 14 04:55:33 with the six photometric filters: *uvw*2, *uvm*2, *uvw*1, *u*, *b*, and *v* of the UVOT (Roming et al. 2005). The lower case filter name convention is typically used in this paper for the photometry or spectrophotometry in the UVOT bands. Since the differences are small, no corrections are made to the standard Johnson *B* and *V* filters, and upper case letters are sometimes used to match common usage, such as $\Delta m_{15}(B)$ or $E(B-V)$. Filter details are available in Roming et al. (2005) and Breeveld et al. (2011). An image of SN 2017erp and its host galaxy is displayed in Figure 1. The photometry was reduced using the pipeline of the *Swift* Optical/Ultraviolet Supernova Archive (SOUSA; Brown et al. 2014a) using the zero-points of Breeveld et al. (2011) on the Vega system. The *Swift*/UVOT reduction includes the subtraction of the host galaxy count rate in the UVOT filters using observations taken about 16 months after the SN explosion. The difference between the peak magnitudes with subtraction and no subtraction at all is less than 0.02 mag in the optical using a 3″ aperture. The subtraction of the host galaxy has the strongest impact in the *uvm*2 filter, equal to 0.25 mag. The final photometric errors include the propogation of the statistical uncertainty of the SN +galaxy and galaxy count rates and a 2% systematic uncertainty on each due to large-scale sensitivity differences across the detector.

The light curves are shown in Figure 2 and the magnitudes listed in Table 1. The extremely red early colors prompted us to trigger our *HST* program once we had confidence that the colors were not solely due to dust reddening and that SN 2017erp would be bright enough in the mid-UV to obtain useful spectra. This assessment was done using color evolution and color–color evolution plots of young SNe Ia previously observed with *Swift*/UVOT as well as the UV/optical spectral

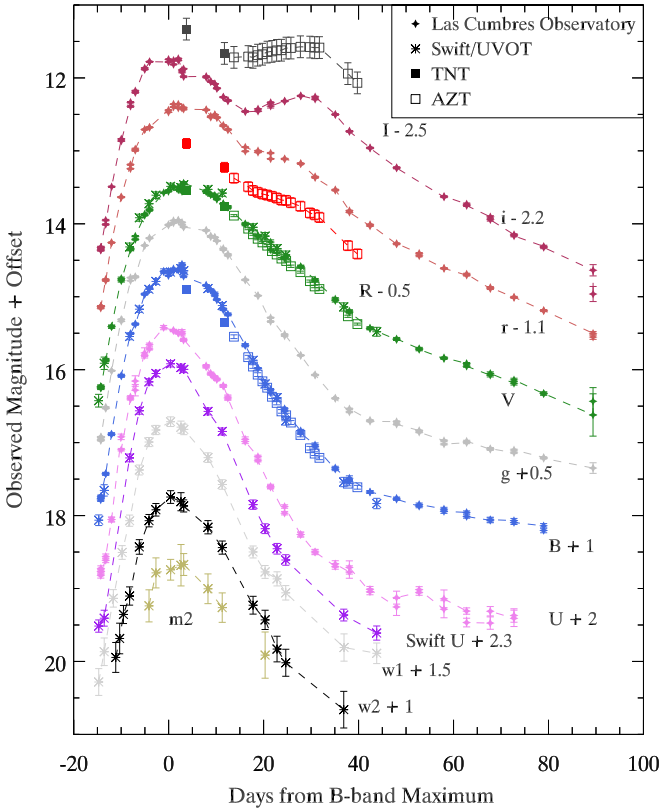

Figure 2. Photometry of SN 2017erp from the *Swift*/UVOT, the Las Cumbres Observatory network, Xinglong Observatory's Tsinghua-NAOC 0.8 m telescope (TNT), and the Madanak Astronomical Observatory's AZT.

template of SN 2011fe (Pereira et al. 2013) with different amounts of reddening applied to map out the parameter space covered by a reddened NUV-blue SN Ia (Brown et al. 2017).

2.3. HST/*Space Telescope Imaging Spectrograph (STIS) Spectroscopy*

Observations with the *HST* were triggered as part of the program "Ultraviolet Spectra of a Normal Standard Candle" to obtain UV spectroscopy. Four epochs were obtained with the *HST*'s STIS using the G430L grism and the CCD detector and the G230L grism and the MAMA detector. For these spectra we use the default *HST* reduction obtained from the Mikulski Archive for Space Telescopes.[22] We eliminate bad pixels and cosmic rays, smooth the spectra in 5 Å bins, and combine the MUV G230L and NUV/optical G430L spectra. The four epochs are displayed in Figure 3 with observation times listed in Table 2.

2.4. *Ground-based Optical Photometry*

Optical light curves and spectra come from the Global Supernova Project, a three-year Key Project to observe light curves and spectroscopy of hundreds of SNe using the Las Cumbres Observatory global network of 21 robotic telescopes. *UBVgri* images were taken with the Sinistro cameras on the Las Cumbres Observatory network of 1 m telescopes (Brown et al. 2013). Point-spread function (PSF) photometry was extracted using `lcogtsnpipe` (Valenti et al. 2016), a PyRAF-based photometric reduction pipeline. *UBV* Vega magnitudes are

[22] https://archive.stsci.edu/hst/

Table 1
Photometric Magnitudes of SN 2017erp

MJD (days)	Magnitude (mag)	Filter	Observatory
57918.25	16.43 ± 0.09	*v*	UVOT
57918.27	18.78 ± 0.18	*uvw1*	UVOT
57918.27	17.21 ± 0.08	*u*	UVOT
57918.27	17.06 ± 0.07	*b*	UVOT
57918.69	16.77 ± 0.02	*B*	LCO
57918.69	16.79 ± 0.02	*B*	LCO
57918.70	16.26 ± 0.01	*r*	LCO
57918.70	16.23 ± 0.01	*r*	LCO
57918.70	16.25 ± 0.02	*V*	LCO
57918.70	16.23 ± 0.02	*V*	LCO
57918.71	16.56 ± 0.01	*i*	LCO
57918.71	16.56 ± 0.01	*i*	LCO
57918.71	16.82 ± 0.03	*u*	LCO
57918.71	16.77 ± 0.03	*u*	LCO
57918.72	16.45 ± 0.01	*g*	LCO
57918.72	16.47 ± 0.01	*g*	LCO
57918.73	16.24 ± 0.02	*V*	LCO
57918.73	16.25 ± 0.02	*V*	LCO
57918.73	16.52 ± 0.01	*i*	LCO
57918.73	16.52 ± 0.01	*i*	LCO
57918.73	16.72 ± 0.03	*u*	LCO
57918.74	16.77 ± 0.04	*u*	LCO
57918.74	16.42 ± 0.01	*g*	LCO
57918.74	16.42 ± 0.01	*g*	LCO
57918.75	16.23 ± 0.01	*r*	LCO
57918.75	16.23 ± 0.01	*r*	LCO
57918.75	16.74 ± 0.02	*B*	LCO
57918.75	16.73 ± 0.02	*B*	LCO
57919.42	18.37 ± 0.19	*uvw1*	UVOT
57919.42	17.11 ± 0.11	*u*	UVOT
57919.42	16.66 ± 0.08	*b*	UVOT
57919.43	15.91 ± 0.09	*v*	UVOT
57919.74	16.42 ± 0.02	*B*	LCO
57919.74	16.43 ± 0.02	*B*	LCO
57919.74	16.15 ± 0.01	*i*	LCO
57919.74	16.21 ± 0.01	*i*	LCO
57919.75	15.86 ± 0.01	*r*	LCO
57919.75	15.88 ± 0.01	*r*	LCO
57919.75	16.61 ± 0.03	*u*	LCO
57919.75	16.56 ± 0.03	*u*	LCO

(This table is available in its entirety in machine-readable form.)

calibrated to Landolt standard fields taken at the same site and on the same night as observations of the SN. *gri* AB magnitudes are calibrated to the Sloan Digital Sky Survey.

Broadband *BVRI*-band photometric observations of SN 2017erp were also obtained with the Tsinghua-NAOC 0.8 m telescope (TNT) at Xinglong Observatory in China (Huang et al. 2012) and AZT-22 1.5 m telescope (hereafter AZT) at Madanak Astronomical Observatory in Uzbekistan, spanning the phases from +2 to +28 days relative to the *B*-band maximum light. All CCD images were preprocessed using standard routines, which include corrections for bias, flat field, and removal of cosmic rays. As the SN is located relatively far from the galactic center, we did not apply a technique of subtracting the galaxy template from the SN images; instead, the foreground sky was determined locally using a nearby annulus and subtracted. The instrumental magnitudes of both the SN and the reference stars were then measured using the standard PSF. These magnitudes are converted to those of the standard Johnson-Vega system using the APASS catalog.[23]

2.5. Optical Spectroscopy

Spectra were taken with the robotic FLOYDS spectrographs on Las Cumbres Observatory's 2 m telescopes on Haleakalā Hawai'i, and in Siding Spring, Australia, and were reduced using the PyRAF-based `floydsspec` pipeline. Additional spectra were taken with the Southern African Large Telescope (SALT) using the Robert Stobie Spectrograph (Smith et al. 2006) as part of program 2017-1-MLT-002 (PI: Jha). We used the PG0900 grating and 1.″5 longslit, yielding a spectral resolution $\lambda/\Delta\lambda \approx 900$ over the wavelength range 3500–9400 Å. The data were reduced with a custom pipeline that incorporates routines from PyRAF and PySALT[24] (Crawford et al. 2010). A series of spectra of SN 2017erp also were obtained with the Xinglong 2.16 m telescope (XLT +BFOSC) of NAOC, China, the 2.3 m Australian National University (ANU) telescope (+WiFeS), and the 6.5 m Magellan telescope (+IMACS). All of the spectra were mangled to match the *BVgri* photometry at that epoch, except for the first SALT spectrum, which predated the photometry. The optical spectra are displayed in Figure 4, and the observation dates and wavelength ranges of all the spectra are given in Table 2.

2.6. Gemini NIR Spectroscopy

One epoch of NIR spectroscopy was obtained with the FLAMINGOS-2 (Eikenberry et al. 2008) spectrograph at Gemini South on 2017 July 11. The FLAMINGOS-2 data were taken with the JH grism and filter in place, along with a 0.72 arcsec slit width, yielding a wavelength range of 1.0–1.8 μm and $R \sim 1000$. The FLAMINGOS-2 longslit data were reduced in a standard way (i.e., image detrending, sky subtraction of the AB pairs, spectral extraction, spectral combination, and wavelength calibration) using the F2 pyraf package provided by the Gemini Observatory. An A0V star was observed near in time and position to the science data in order to make a telluric absorption correction and to flux calibrate the spectra, following the methodology of Vacca et al. (2003). This spectrum is compared to a GNIRS NIR spectrum of SN 2011fe (Hsiao et al. 2013) in Figure 5.

3. Analysis

3.1. Light-curve Parameters

We used the SuperNovae in object-oriented Python (SNooPy; Burns et al. 2011) light-curve fitter on the Las Cumbres Observatory BVgri photometry to determine various light-curve parameters. The *B* band reached a maximum brightness of 13.27 ± 0.01 mag on MJD 57,934.9 (UT 2017 June 30.9). Δm_{15}, a parameterization of the multifilter templates sorted by $\Delta m_{15}(B)$, is measured to be 1.05 ± 0.06, while $\Delta m_{15}(B)$ directly measured from the UVOT light curves is 1.11 ± 0.02. SNe Ia with $1.0 < \Delta m_{15}(B) < 1.4$ would be considered normal, with $\Delta m_{15}(B) = 1.1$ usually used as the reference value (e.g., Phillips et al. 1999). The color stretch (Burns et al. 2014) measured with SNooPy is $s_{BV} = 0.993 \pm 0.03$. For comparison, an SN with $\Delta m_{15}(B) = 1.1$

[23] https://www.aavso.org/apass
[24] http://pysalt.salt.ac.za/

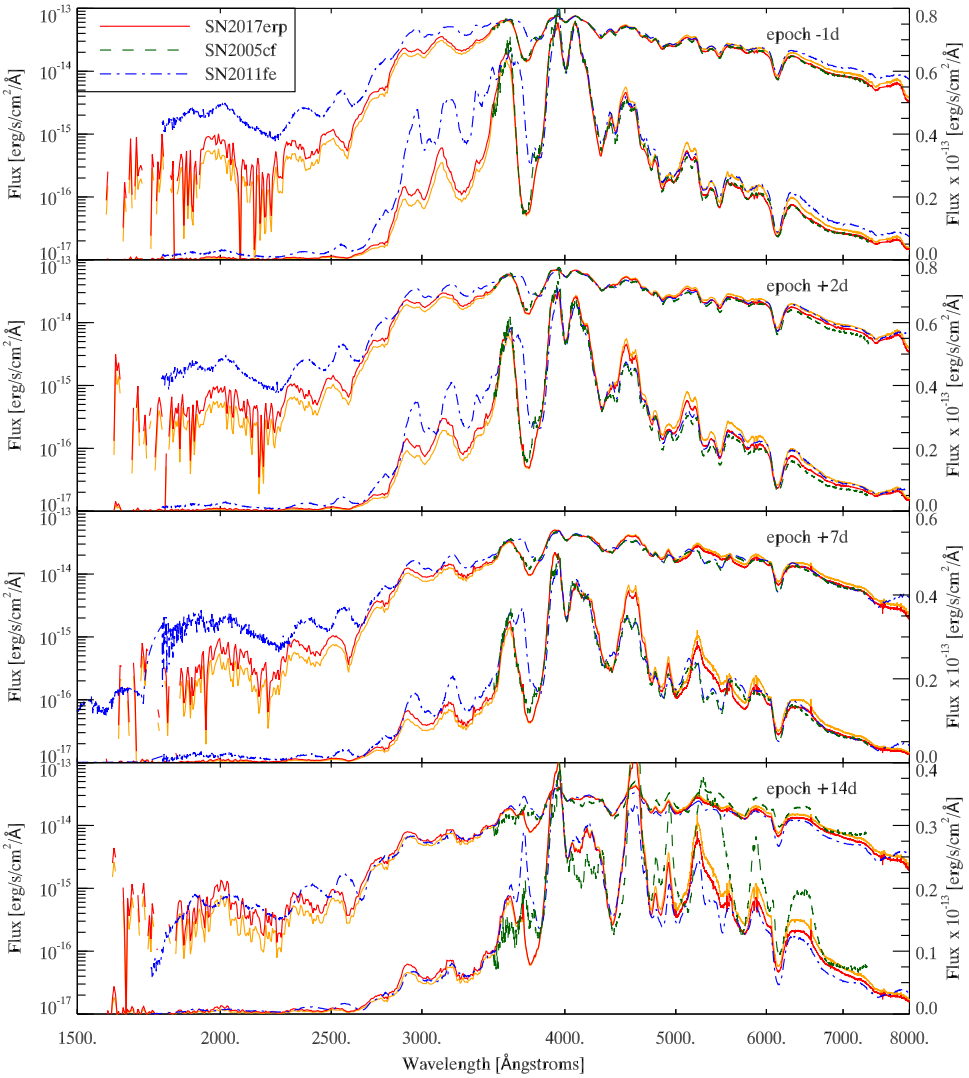

Figure 3. Four epochs of SN 2017erp UV spectroscopic observations (combined with optical spectra from nearby epochs and corrected for MW and host reddening (host $E(B-V) = 0.1$ and 0.18) are compared with SNe 2005cf and 2011fe. The observed flux is displayed in logarithmic (top curves in each panel with units on the left y-axis) and linear (lower curves with units on the right) scales, with the spectra of the comparison SNe scaled to match SN 2017erp around 4000 Å.

would have a $s_{\rm BV} = 0.95$. Thus SN 2017erp has a very standard light-curve shape.

3.2. Reddening and the Intrinsic Color of SN 2017erp

The line-of-sight dust extinction through the Milky Way (MW) is estimated to be $A_V = 0.296$ based on the Schlegel et al. (1998) dust maps recalibrated by Schlafly & Finkbeiner (2011), corresponding to $E(B-V) = 0.095$ mag, assuming $R_V = 3.1$. The optical spectra show absorption by interstellar Na I D from both the Milky Way and the host galaxy NGC 5861 with comparable strengths. Our best optical spectrum (in terms of signal-to-noise and resolution in that region), the SALT spectrum taken 6 days after maximum light, is used to measure the EW of both components. Using a variety of places on the spectrum to set the continuum level and estimate the uncertainty, we measure EWs of 0.65 ± 0.05 and 0.77 ± 0.06. This corresponds to $E(B-V) = 0.09$ for the MW component, consistent with the Schlafly & Finkbeiner (2011) determination, using the correlation of Poznanski et al. (2011). The host component corresponds to $E(B-V) = 0.11 \pm 0.03$. It is actually the extinction A_V that should correlate with the Na ID EW Phillips et al. (2013), but we are making an implicit assumption that the relevant host galaxy properties (dust to gas ratio, R_V, etc.) are similar to the MW.

For other estimates of the total reddening, we compare the $B_{\rm peak}$–$V_{\rm peak}$ pseudocolor to Equation (7) of Phillips et al. (1999), yielding a host $E(B-V)$ of 0.13 mag. By the term pseudocolor we refer to the subtraction of the nonsimultaneous peak magnitudes in different filters, while the peak color would refer to the subtraction of magnitudes at the time of maximum light in the B-band light curve. An alternative estimate of the reddening comes by comparing $B-V$ colors between 30 and 90 days after the time of V-band maximum to the Lira relation (Phillips et al. 1999), which is a linear fit to the fairly uniform color decay of SNe Ia. The host $E(B-V)$ color excess measured for individual observations compared to the Lira relation after correction for the MW component has an mean of 0.16 mag and a standard deviation of 0.03 mag.

Light-curve fitters such as MLCS2k2 (Jha et al. 2007), SNooPy (Burns et al. 2011), and SALT2 (Guy et al. 2010) use more of the light curve in determining the color differences,

Table 2
Spectroscopic Observations of SN 2017erp

Epoch (days)	UT Time 2017 (mm dd hh:mm:ss)	Instrument	λ Start (Å)	λ End (Å)
−17.0	Jun 13 22:14:34	SALT/RSS	3497	9400
−16.3	Jun 14 14:45:03	XLT/BFOSC	3902	8790
−16.2	Jun 14 17:55:06	SALT/RSS	3495	9398
−15.1	Jun 15 18:08:17	SALT/RSS	3493	9397
−14.1	Jun 16 18:03:51	SALT/RSS	3496	9397
−13.3	Jun 17 14:49:53	XLT/BFOSC	4001	8779
−12.1	Jun 18 18:04:46	SALT/RSS	3497	9398
−10.4	Jun 20 12:54:50	ANU/WiFeS	3351	9500
−10.2	Jun 20 17:52:04	SALT/RSS	3495	9397
−8.5	Jun 22 09:29:26	LCO/Floyds	3501	10000
−5.5	Jun 25 08:31:00	ANU/WiFeS	3351	9001
−4.3	Jun 26 13:57:44	LCO/Floyds	3300	10000
−1.5	Jun 29 10:24:23	*HST*/STIS/CCD	3000	5600
−1.4	Jun 29 12:33:45	*HST*/STIS/MAMA	1585	3135
−1.0	Jun 29 21:51:55	SALT/RSS	3497	9400
−0.4	Jun 30 11:54:32	LCO/Floyds	3299	10000
0.0	Jun 30 21:44:16	SALT/RSS	3496	9400
1.6	Jul 2 11:26:15	*HST*/STIS/CCD	3000	5600
1.6	Jul 2 11:26:15	*HST*/STIS/MAMA	1585	3135
5.6	Jul 6 11:56:05	LCO/Floyds	3851	9298
6.0	Jul 6 20:50:57	SALT/RSS	3499	9399
6.3	Jul 7 05:43:08	*HST*/STIS/CCD	3000	5600
6.4	Jul 7 07:41:15	*HST*/STIS/MAMA	1585	3135
10.2	Jul 11 02:26:15	G-S/FLAM2[a]	9860	18000
10.5	Jul 11 09:45:07	ANU/WiFeS	3300	9499
11.2	Jul 12 01:41:15	*HST*/STIS/CCD	3000	5600
11.3	Jul 12 05:15:00	*HST*/STIS/MAMA	1585	3135
11.4	Jul 12 08:16:09	LCO/Floyds	3551	9200
14.4	Jul 15 07:12:04	LCO/Floyds	3901	8898
15.4	Jul 16 06:51:48	LCO/Floyds	3500	10000
16.6	Jul 17 10:51:17	ANU/WiFeS	3601	9489
17.0	Jul 17 20:36:51	SALT/RSS	3497	9400
22.5	Jul 23 08:37:29	LCO/Floyds	3901	8799
27.6	Jul 28 11:03:13	LCO/Floyds	3901	8800
37.4	Aug 7 06:30:13	LCO/Floyds	3902	10001
40.3	Aug 10 05:51:04	LCO/Floyds	3402	10000
45.5	Aug 15 08:35:38	ANU/WiFeS	3801	9198
69.1	Sep 8 00:10:38	Magellan/IMACS	4161	9343

Note.
[a] Gemini-South/FLAMINGOS-2.

and thus reddening, between the SN Ia being fit and the training sample.

The MLCS2k2 (Jha et al. 2007) fit to the optical BVri light-curve data with Milky Way $E(B-V) = 0.095$ yields $\Delta = -0.19 \pm 0.02$ and host $A_V = 0.39 \pm 0.04$ for fixed host $R_V = 1.9$. This corresponds to a host $E(B-V) = 0.21 \pm 0.02$ and thus a total $E(B-V) = 0.31$. The MLCS2k2 distance modulus is 32.22 ± 0.09 (on an $H_0 = 72\,\mathrm{km\,s^{-1}\,Mpc^{-1}}$ scale), marginally consistent with the Hubble flow distance modulus of 32.30 mag. A fit that included U and g resulted in poor fits in those filters and pulled the fit to a higher host $E(B-V) = 0.29 \pm 0.02$ and a closer distance modulus of 32.07 ± 0.09. This could be due to differences between the filter transmission curves used in the observations and those used for training similar filters or the strong Ca H&K feature being interpreted as reddening.

The color model of SNooPy estimates the $E(B-V)_{\rm host} = 0.179 \pm 0.005$ (statistical) ± 0.060 (systematic) mag with $R_V = 2.80 \pm 0.51$. Fitting similar to Prieto et al. (2006) yields

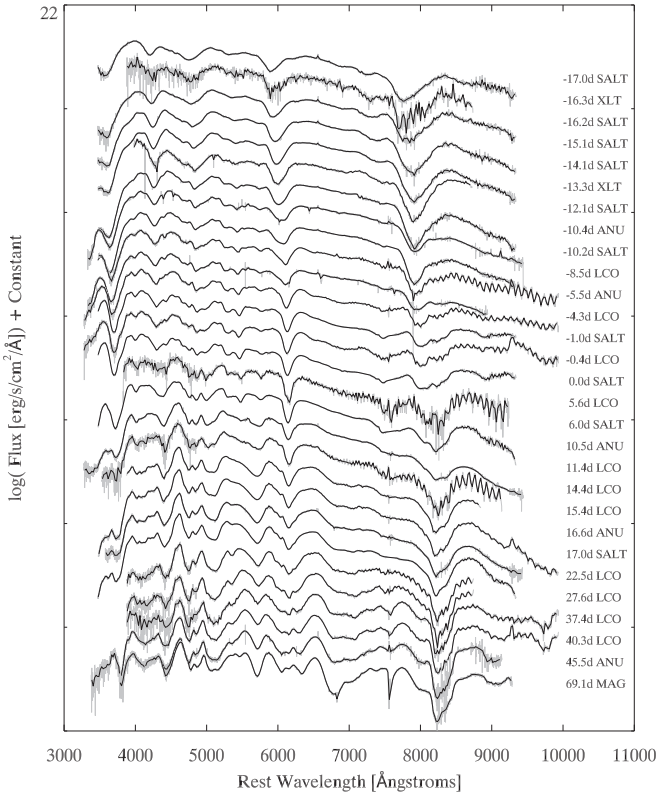

Figure 4. Optical spectral series of SN 2017erp presented in the rest frame of SN 2017erp. Original spectra (with some regions of low S/N trimmed out) are plotted in gray. A smoothed version of the spectra (10 Å bins) is plotted in black. Except for the first spectrum, all have been modified (i.e., warped or mangled) using a low-order polynomial to match the photometry.

$E(B-V)_{\rm host} = 0.097 \pm 0.005$ (statistical) ± 0.060 (systematic) mag, assuming $R_V = 3.1$.

The optical light curves were also fit with the SALT2 model (Guy et al. 2010) using the SNCosmo package (Barbary et al. 2016). The best-fit parameters are $m_B = 13.28$, $x_1 = 0.46$, and $c = 0.05$, where m_B is the peak magnitude at rest frame B band, x_1 is the shape parameter and c is the color parameter. Using the Tripp relation (Tripp 1998): $\mu = m_B + \alpha x_1 - \beta c - M$ and setting $\alpha = 0.14$, $\beta = 3.1$, and $M = -19.1$, we determine the distance modulus as 32.29 ± 0.12, where the uncertainty has been estimated based on the typical scatter for SN Ia. The SALT2 color term does not translate directly into a host reddening $E(B-V)$ because it empirically combines intrinsic color as well as the dust reddening. The distance modulus is consistent with the MLCS2k2 distance modulus. Vinkó et al. (2012, 2018) found that $\leqslant 0.2$ mag differences are possible between the distance modulus determinations for well-observed SNe as determined by different fitting methods and using the same method on separate subsets of *BVRI* and $g'r'i'z'$ data.

The various reddening estimates are summarized in Table 3. Clearly there are differences larger than the claimed uncertainties. Since the difference would be due to systematic uncertainties in the fitting techniques or the filters used, instead of averaging or otherwise combining the values we will instead present the results for different assumptions in the host galaxy reddening, utilizing either all of the values or two values representing the clusters of values, namely host $E(B-V) = 0.10$ and 0.18, with $R_V = 3.1$ and 1.9, respectively.

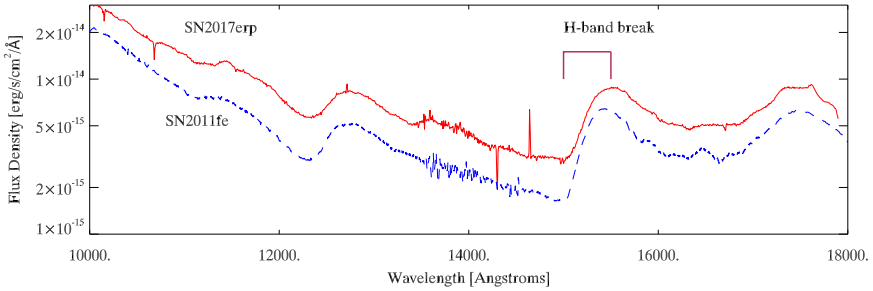

Figure 5. NIR spectra of SNe 2017erp (10 days after *B*-band maximum) and 2011fe (9 days after *B*-band maximum; Hsiao et al. 2013) are compared. SN 2017erp has been reddening corrected based on the MW dust extinction from Schlafly & Finkbeiner (2011) and the host color excess from SNooPy.

Table 3
Reddening Estimates of SN 2017erp

Reddening Method	$E(B-V)$	R_V
NaI D	0.11 ± 0.03	···
Peak Color	0.13 ± 0.03	···
Lira Law	0.19 ± 0.03	···
MLCS2k2	0.21 ± 0.01	[1.9[a]]
Snoopy Prieto	0.10 ± 0.06	[3.1[a]]
SNooPy Color Model	0.18 ± 0.06	2.80 ± 0.51
SNooPy Color Model MCMC	0.18 ± 0.03	1.93 ± 0.81

Note.
[a] R_V is assumed, not fit.

The observed color evolution and peak maximum light colors of SN 2017erp are consistent with the NUV-red SNe Ia as defined by Milne et al. (2013). Figure 6 shows the $uvw1-v$ color evolution compared to shaded regions representing the NUV-blue and NUV-red groups (Brown et al. 2017). This definition utilized the observed colors and did not take into account dust reddening.

As shown in Brown et al. (2017), however, some SNe Ia with observed colors similar to NUV-red SNe could be NUV-blue SNe reddened by dust. Determining the intrinsic colors is complicated by the possibility of different intrinsic optical colors (Milne et al. 2013), uncertainty in the appropriate dust reddening law, and how much the intrinsic spectral differences would affect the broadband filter extinction coefficients determined from a NUV-blue spectral template like SN 2011fe. The latter uncertainty is removed by having a new spectral sequence of a NUV-red SN Ia. In Figure 6 we also plot the spectrophotometric color evolution from the *HST* observations with different amounts of reddening applied. With the larger host $E(B-V)=0.18$ inferred from the multiband data, SN 2017erp crosses into the color evolution space occupied by NUV-blue SNe Ia. The $B-V$ evolution in such a case becomes bluer than the unreddened SN 2011fe template.

In Figure 7 we focus on the peak color of SN 2017erp and compare with those of the Brown et al. (2017) sample with $1.0<\Delta m_{15}(B)<1.4$. Lines show the reddening vectors for SN 2011fe and SN 2017erp corresponding to different dust reddening laws. The dust reddening laws include the Cardelli et al. (1989) law parameterized with $R_V=3.1$ (like the MW) and $R_V=1.7$ (similar to that found for SNe Ia; e.g., Kessler et al. 2009), an extinction law measured for the SMC (Prevot et al. 1984), and a Large Magellenic Cloud extinction law modified by circumstellar scattering (Goobar 2008; Brown et al. 2010). We also show symbols corresponding to dereddening the SN 2017erp spectrum for MW reddening

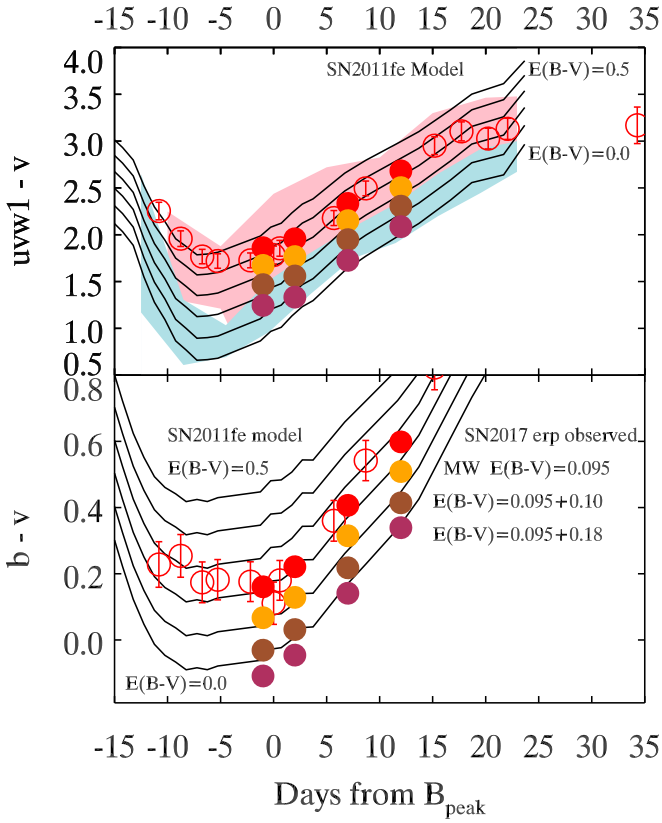

Figure 6. Observed and reddening-corrected $uvw1-v$ and $b-v$ color evolutions of SN 2017erp are compared with regions occupied by SNe Ia identified as NUV-red (pink shaded region) and NUV-blue (blue shaded region) by Milne et al. (2013) and a spectroscopic model of SN 2011fe (Pereira et al. 2013) with different amounts of reddening applied (represented by solid curves). The photometric observations of SN 2017erp are indicated by open circles. Filled circles show the spectrophotometric colors from the *HST* observations of SN 2017erp with various amounts of reddening applied (the same color circles are used in both panels and labeled in the bottom panel). For the largest amount of reddening, SN 2017erp has colors most similar to the NUV-blue group, but the $B-V$ color is also bluer than the SN 2011fe template.

with $E(B-V)=0.095$ mag and $R_V=3.1$ and after correcting for the MW reddening and the SNooPy estimated host reddening of $E(B-V)=0.097$ mag (with $R_V=3.1$).

For a host reddening of $E(B-V)=0.1$, the dereddened colors of SN 2017erp are about 0.5 mag redder in the $uvw1-v$ color than the low reddened SN 2011fe, with comparable colors to several NUV-red SNe Ia. For the larger host reddening of $E(B-V)=0.18$, the $uvw1-v$ color becomes comparable to the NUV-blue SN2011by. The dereddened $B-V$ color, however, would be significantly bluer than the

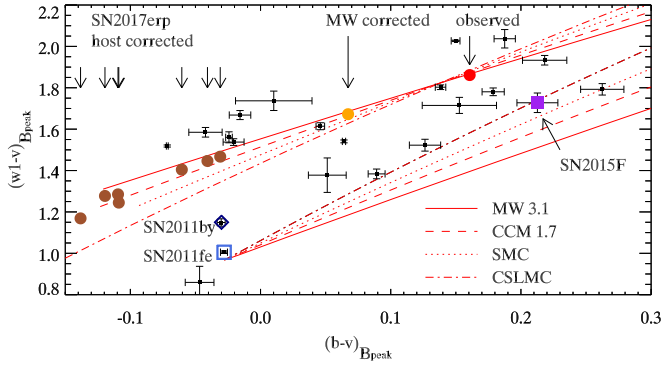

Figure 7. Observed peak colors of normal SNe Ia observed with *Swift* plotted as small black points with error bars. SNe Ia observed with *HST* are designated with a solid red circle (SN 2017erp), solid purple square (SN2015F), open diamond (SN 2011by), and open square (SN 2011fe). Red lines show the color–color vectors of SN 2011fe reddened and SN 2017erp reddened and dereddened with various reddening laws to show which of the observed SNe could have similar intrinsic colors and only differ by being more or less reddened. SN 2017erp is shown as observed (red circle), dereddened by the MW extinction (orange circle), and dereddened for various host reddening estimates (brown circles), with downward pointing arrows at the $b-v$ color of each. The original horizontal division line between NUV-blue and NUV-red is ∼1.2 (Milne et al. 2013) and did not consider the effect of reddening. Intrinsic NUV-optical color variations would cause variations in the vertical spread in $uvw1-v$ for objects with similar $B-V$ color (though optical color differences could cause the intrinsic colors to have a slope in a plot such as this). In this color–color plot, SN 2017erp is offset from the NUV-blue SNe 2011by and 2011fe in a direction perpendicular to the reddening vectors and closer to several objects that are optically blue ($b-v\sim-0.05$) but much redder with $uvw1-v\sim1.6$. We are thus confident that intrinsically SN 2017erp is more similar to the NUV-red SNe Ia.

observed colors of the other SNe. This is understandable as the SNooPy fitting seeks to correct the colors to match the bluest in the CSP training sample. In this case, the $B-V$ color at peak ends up about one σ bluer than the mean for objects of similar light-curve stretch (Burns et al. 2014). It would be the bluest SN Ia of the *Swift* sample in both colors. The reddening estimated from the peak $B-V$ colors is smaller than that from the whole light-curve fitters or the late-time Lira relation, so the larger estimates push the reddening-corrected peak color bluer.

Though SN 2017erp could be dereddened enough to be close in $uvw1-v$ color to those observed for some NUV-blue SNe Ia, its dereddening tracks in the color–color diagram are most consistent with the NUV-red SNe. A clear understanding of the intrinsic colors would require a correct dust reddening correction for the sample—a correction that might depend on the intrinisic spectral shape. Brown et al. (2017) considered the perpendicular offset from SN 2011fe's reddening vector as a more appropriate measure of the intrinsic UV differences than simply the NUV-optical color used by Milne et al. (2013). However, an intrinsic difference in $B-V$ colors correlated with the NUV colors (Milne et al. 2013; possibly due to metallicity Höflich et al. 1998; Walker et al. 2012) is also a possible complication. The histogram of colors offset from the SN2011fe with MW dust reddening vector in Brown et al. (2017) showed less of a dichotomy in the NUV colors. In that paradigm, the colors range from 0 (SN2011fe) to 0.8 mag, with SN 2017erp near 0.5. Though not at the extreme red end, this makes the SN 2017erp *HST* spectral series complementary to those of the NUV-blue SNe 2011fe (Mazzali et al. 2014) and 2011by (Foley & Kirshner 2013) and the reddened NUV-blue SN 2015F (Foley et al. 2016). A diversity in spectral templates to match the observations is important regardless of whether

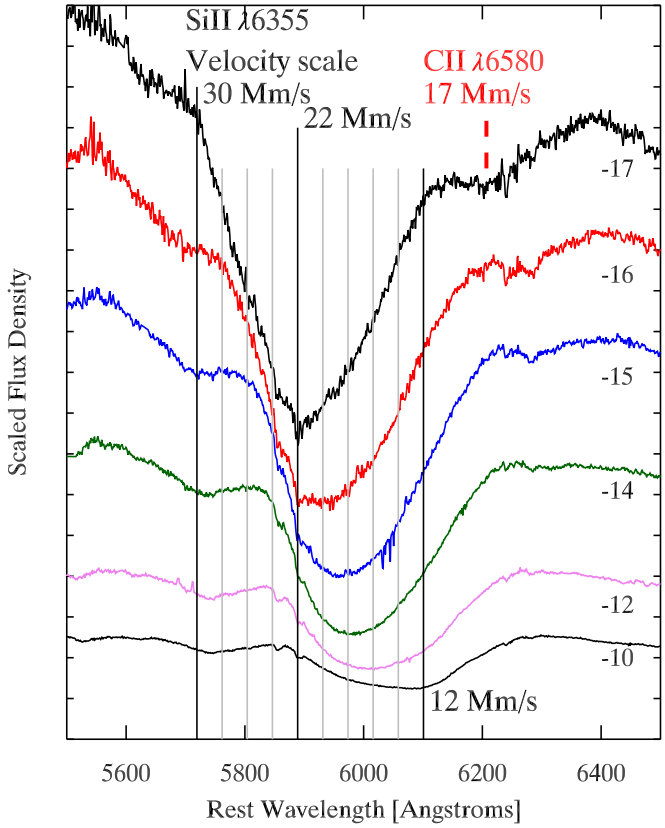

Figure 8. Portion of the early SALT optical spectra covering 17–10 days before maximum light. The earliest spectrum, taken 17 days before maximum light, shows Si II with a photospheric velocity of 22 Mm s^{-1} and with a blue wing extending to at least 30 Mm s^{-1}. The −10 day spectrum shows a flattened Si II feature, a superposition of the fading high-velocity Si II feature and the emerging photospheric Si II. A clear absorption feature from C II is visible in at least the first three spectra but is gone 12 days before maximum light.

the SNe Ia at the NUV-blue and NUV-red ends represent distinct groups or a continuously varying color difference.

3.3. Spectroscopic Comparisons

3.3.1. Optical Spectra

The full optical spectral evolution of SN 2017erp is shown in Figure 4, while Figure 8 focuses on the region of the Si II 6355 Å line in the early spectra. The velocity of the Si II 6355 Å absorption begins at a high velocity of 21.5 Mm s^{-1} (Jha et al. 2017) but drops quickly to a value of 10.4 Mm s^{-1} at maximum light. The early velocity is actually that of a high-velocity component. The asymmetric Si II profile 11 days before maximum light shows the transition between the feature being dominated by the high-velocity component to being dominated by the photospheric component. SN 2009ig showed similar behavior, and Marion et al. (2013) measured the velocity evolution of the separate components. Figure 9 shows the velocity evolution of the Si II 6355 line (considering only the dominant component) and demonstrates SN 2017erp is not significantly different from the "gold standards" SNe 2011fe (Pereira et al. 2013; Zhang et al. 2016) and 2005cf (Garavini et al. 2007; Pastorello et al. 2007; Wang et al. 2009b) in terms of photospheric velocity evolution. At shorter wavelengths, the Ca II H&K feature also begins by being very broad and stretched to blue wavelengths. By day 15 (though probably earlier where our spectra are noisier) the Ca II H&K feature is

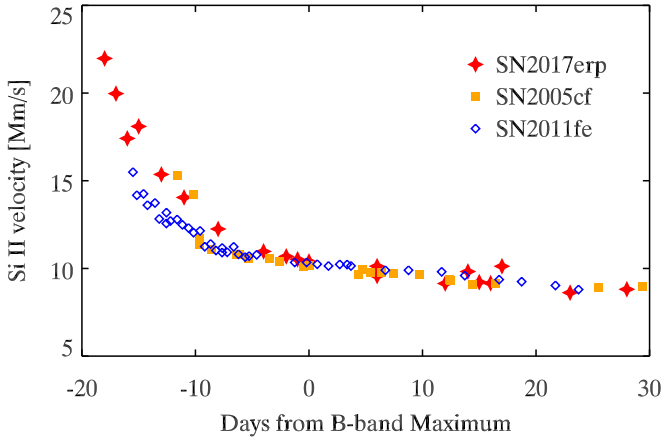

Figure 9. Photospheric velocity of SN 2017erp is compared to SNe 2005cf and 2011fe, showing a similar behavior and value near maximum light.

split into two distinct features with a high-velocity feature at a similar velocity as near maximum light.

Milne et al. (2013) found that SNe Ia with high velocities (HV; Si II ejecta velocities greater than about 12 Mm s^{-1} Wang et al. 2009a) are almost exclusively NUV-red, while normal-velocity SNe Ia can be either NUV-red or NUV-blue. Meanwhile, the NUV-blue SNe Ia all have velocities below 12 Mm s^{-1}. Brown et al. (2018) confirmed this, showing that SNe Ia with normal velocities have a range of UV colors with no correlation with the velocities. Thus the photospheric velocity does not differentiate NUV-red and NUV-blue SNe Ia, consistent with the optical similarities seen here. However, the similarity in the high-velocity features of SNe 2017erp and 2005cf suggest a possibility that high-velocity features may be related to the similar NUV-red colors. This would be consistent with the high-velocity features and the UV continuum both arising from the outer layers of the SN ejecta. Brown et al. (2018) found that the asymmetric models of Kasen & Plewa (2007) did not reproduce the observed UV colors, but further work modeling asymmetry (e.g., Maeda et al. 2010; Maund et al. 2010) and its effect on the UV (e.g., Kromer & Sim 2009; Brown et al. 2014b will better constrain how much of an effect asymmetry could have on the UV colors.

Milne et al. (2013) also found that all of their NUV-blue SNe Ia had carbon detected in their spectra. The majority of NUV-red SNe Ia had no detections, with SN 2005cf as the lone exception. SN 2017erp would be another exception, as it shows strong C II absorption in the earliest spectrum. This is shown in Figure 8. However, the C II is gone by the fifth spectrum, taken 12 days before maximum light. If the earlier spectra had not been taken, the spectrum 12 days before maximum would have counted as a nondetection. C II was detected in SN 2005cf eleven days (Silverman & Filippenko 2012) and 9.4 days maximum light (Thomas et al. 2011) and then not detected two days later. These two exceptions might be due to how early the observations of SNe 2005cf and 2017erp began. Other NUV-red SNe may have had detectable carbon had they been observed at similarly early epochs. A better understanding of the relationship between carbon and UV colors would require both to be treated as continuous parameters (which each change with time) rather than individual classes.

3.3.2. Near-infrared Spectrum

Figure 5 compares the NIR spectrum of SN 2017erp at 10.2 days after maximum light with SN 2011fe at a comparable epoch. The SN 2011fe spectrum is from a Gemini GNIRS near-infrared spectrum from Hsiao et al. (2013). The Gemini spectrum of SN 2017erp was conveniently taken near the epoch when the H-band break near 1.5 μm is strongest. Dividing the peak flux on the long side of the break by the minimum flux on the short wavelength side, we calculate the H-band break ratio $R_{12} = 3.0 \pm 0.1$. This is lower than SN 2011fe (3.9; Hsiao et al. 2013), but consistent with SN 2005cf (3.1; Hsiao et al. 2013). This fits in the correlation between H-band break ratio and light-curve parameter found by Hsiao et al. (2013, 2015), in which objects with $0.8 < \Delta M_{15}(B) < 1.2$ have R_{12} between 3 and 4, while faster-declining SNe Ia have decreasing values of R_{12} down to $\sim$2 for SN 1999by.

3.3.3. Ultraviolet Spectra

Having established SN 2017erp as having colors similar to the NUV-red SNe Ia, we wish to compare directly the UV spectroscopic properties between the NUV-red and NUV-blue groups with these high-quality *HST* spectra. Previous comparisons in these regions have used lower S/N spectra from UVOT, *HST*'s ACS grism, and ground-based optical spectra of higher redshift SNe Ia (Ellis et al. 2008; Foley et al. 2008a; Cooke et al. 2011; Maguire et al. 2012; Wang et al. 2012; Milne et al. 2013, 2015; Smitka 2016). *HST* spectra in the near-UV covered this region for a sample of SNe Ia (Cooke et al. 2011; Maguire et al. 2012). As shown in Figure 3, the spectral shapes and features near maximum light of SNe 2017erp, 2011fe, and 2005cf are nearly identical longward of 4000 Å. SNe 2005cf and 2017erp continue to be similar in the Ca H&K feature (which is not solely Ca H&K, see e.g., Foley 2013) with a single absorption deeper and bluer than the double feature seen in SN 2011fe. Blueward of that the continuum of SN 2017erp is depressed relative to that of SN 2011fe and instead of two strong peaks as in SN 2011fe, the bluer of the two is basically absent in SN 2017erp. These features are identified as λ_1 and λ_2 in Ellis et al. (2008) and Maguire et al. (2012). The features appear shifted to the blue in SN 2017erp similar to an increase in velocity despite the similar photospheric velocities near maximum light. As explained in Walker et al. (2012), large metallicities will increase the opacity, causing the UV features to appear at even higher velocities (the UV normally forms at higher velocity layers than the optical lines). This is consistent with the near-UV dispersion existing for SNe Ia with low photospheric velocities at peak (Brown et al. 2018). This also makes metallicity, ejecta density gradients, and ejecta velocities linked to each other rather than separate parameters that can be easily distinguished.

The overall flux difference between SNe 2011fe and 2017erp increases at shorter wavelengths into the mid-UV. These are the first spectra revealing the mid-UV properties of a NUV-red SN Ia.

4. Discussion

4.1. Interpreting Intrinsic Ultraviolet Differences as Reddening

Now we examine how the intrinsic differences seen here could be interpreted as peculiar dust extinction. In Figure 10 we

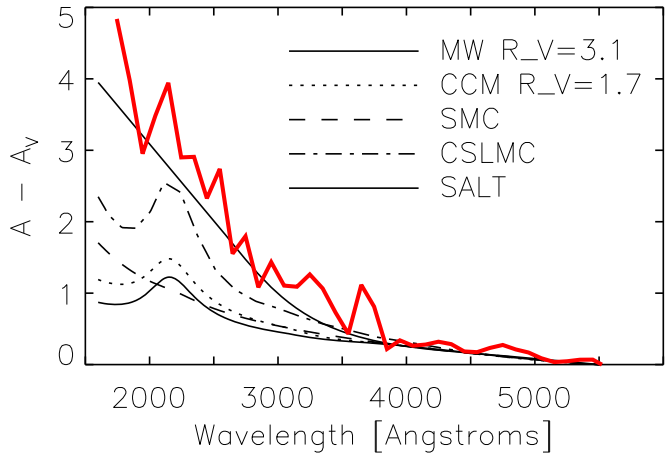

Figure 10. Difference between the spectra of SNe 2011fe and 2017erp in magnitudes is compared to various reddening laws normalized to have the same $B - V$ effect and all shifted to zero in the V band.

compare the difference between SNe 2017erp and 2011fe to the various reddening laws discussed previously and the color law used in the SALT2 light-curve fitter (Guy et al. 2010; Betoule et al. 2014). Because we are interested in the shape of the wavelength dependence, the laws have been scaled to give the same $B - V$ differences as between the SNe and then shifted to zero in the V band. The difference between SNe 2011fe and 2017erp matches broadly the shape of the SALT2 color law (which itself is made from a polynomial fit to broadband observations of higher redshift SNe Ia between 2800–7000 Å and extrapolated to wavelengths above and below that; Guy et al. 2010).

We suggest that in the UV, the steep intrinsic differences could dominate the derivation and use of the SALT2 color law over dust reddening. The SALT2 color law is derived empirically and combines the potential effects of dust reddening and intrinsic color variations. This is difficult to disentangle in the optical, where both dust reddening and intrinsic red color seem to correlate with lower luminosity (e.g., Scolnic et al. 2014). However, the NUV differences do not appear to correlate with luminosity (Maguire et al. 2012; Brown et al. 2017). The use of UV colors to correct for reddening could lead to biased distances especially if the UV colors may change with redshift (Milne et al. 2015; but see also Cinabro et al. 2017).

We have focused on the colors and relative flux levels, as a well-measured distance to the host of SN 2017erp is not yet available. Observations of NGC 5861 with the *HST* have been made with the goal to measure the periods of Cepheid variables (PI: Riess) and calculate a distant in a consistent manner with SNe 2011by, 2011fe, and others (Riess et al. 2016; Foley et al. 2018). This will also shed light on the differences in dust extinction and inferred distance modulus estimated for SN 2017erp by the different light-curve fitters.

4.2. Metallicity as a Possible Origin for the Near-ultraviolet Differences

Understanding the origin of the UV differences is important to better characterizing the progenitors and explosion mechanisms of SNe Ia and how they might change with redshift. Following comparisons from Smitka (2016) that the NUV-blue/red spectral difference between 2700 and 3300 Å (see also Milne et al. 2013, 2015) could be caused by metallicity, we next compare the Walker et al. (2012) models to SNe 2011fe and 2017erp. The Walker models are shown in the left panel of Figure 11. We use a maximum light spectrum of SN 2011fe from Mazzali et al. (2014) and our maximum light spectrum of SN 2017erp dereddened by an MW extinction law with $R_V = 3.1$ and $E(B-V) = 0.2$ mag (for host and MW reddening) and also the spectrum dereddened by $E(B-V) = 0.1$ from the MW and also $E(B-V) = 0.18$ from the host (the latter corrected with an extinction law with $R_V = 1.9$). The spectra are normalized in the optical between 4000 and 4800 Å, so that we can compare the relative flux levels between the optical and the near-UV. The main features in the near-UV are the peaks identified as λ_1 and λ_2 in Ellis et al. (2008) and found by Walker et al. (2012) to be caused by reverse fluorescence. These comparisons are shown in the right panel of Figure 11.

We find a reasonable match between SN 2011fe and the model with one-fifth the metallicity of the baseline model, while SN 2017erp matches the models with a factor of 2–5 increase in metallicity. The comparison plot is similar to that made by Smitka (2016) using *Swift*/UVOT grism spectra of SN 2005df for the NUV-red SN near peak. If the NUV differences are solely due to metallicity and the magnitude of the Walker et al. (2012) models is correct, that would imply a factor of 10 difference in the metallicity between SNe 2011fe and 2017erp. This value should be used with caution, as Mazzali et al. (2014) remark that the Walker et al. (2012) models had a larger fraction of unburned material and thus a stronger dependence on metallicity. Walker et al. (2012) explicitly note that their method of altering the model metallicity cannot distinguish between primordial metallicity of the progenitor and upmixing of products of explosive nucleosynthesis. Distinguishing the two is significant because of the effect of progenitor metallicity on the radioactive output of an SN Ia and thus luminosity (Timmes et al. 2003; Foley et al. 2018).

The uncertainty in the reddening correction does not greatly effect the continuum levels in the near-UV after the normalization in the B band. However, there is also an inconsistency in correcting SNe Ia to have similar optical colors and then comparing them to models with differences in $B-V$ colors. In the Walker et al. (2012) models the SN Ia models with the largest metallicities are 0.1 mag redder than the low metallicity models. The effect of metallicity on SN Ia cosmology is not just a shift in the luminosities (Timmes et al. 2003; Foley et al. 2018) but also the intrinsic colors (Höflich et al. 2000; Podsiadlowski et al. 2006), which affect the extinction corrections and thus the luminosity distances. For this reason it is important to constrain the metallicity effects in SNe Ia for precision cosmology.

Continuing blueward, the mid-UV flux of SN 2017erp falls well below that of SN 2011fe and the best-fitting Walker et al. (2012) model. Foley & Kirshner (2013) have demonstrated using SNe 2011by and 2011fe that SNe with nearly identical optical and near-UV spectra can have very different continuum levels in the mid-UV. They attribute the spectral difference in the mid-UV to be caused by metallicity using the Lentz et al. (2000) models. We do not use the Lentz et al. (2000) models due to the large color difference from actual observations (Brown et al. 2015). Regardless of the cause, the differences between SNe 2011fe and 2011by and SNe 2011fe and 2017erp

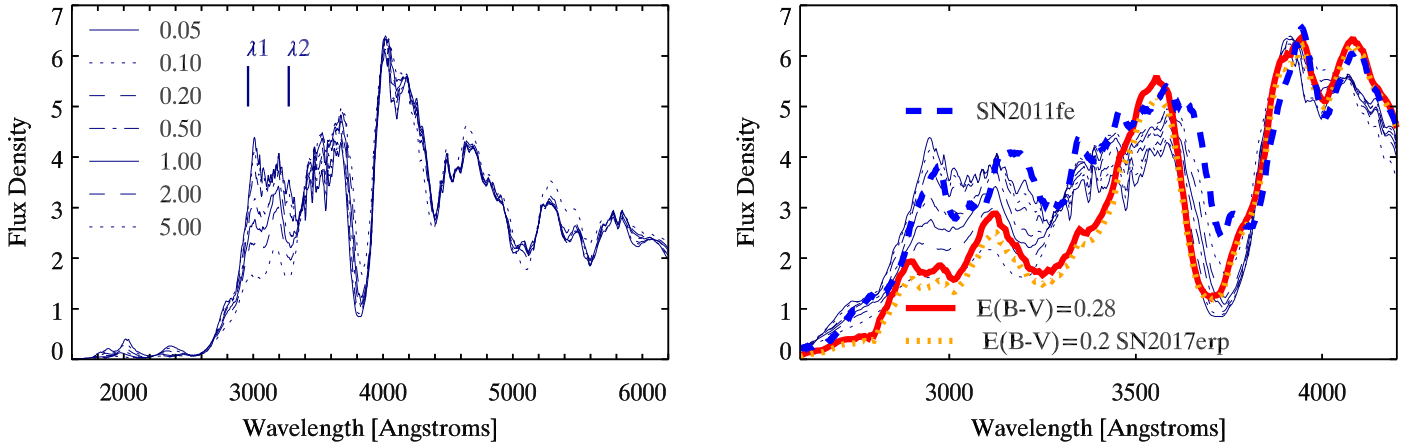

Figure 11. Left panel: maximum light theoretical spectra with varying metallicity from Walker et al. (2012). All of the models shown have the broad Ca H&K feature to match SN 2005cf. The positions of λ_1 and λ_2 identified by Ellis et al. (2008) are also identified. Right panel: the same models are compared to SNe 2011fe and 2017erp, with two different extinction corrections for the latter. SN 2011fe is similar in the near-UV to the model with 0.2 times the metallicity of the baseline model created for SN 2005cf. SN 2017erp is most similar to the models with 2–5 times the metallicity, where the spectra have been normalized in the optical between 4000 and 4800 Å

show that a separate mechanism must affect the mid-UV independent from the near-UV. The Walker et al. (2012) models were not first principle models, nor based on either of these objects, but abundances and density gradients were adjusted to match UV/optical spectra of SN 2005cf near maximum light. Other differences in the spectra are thus not accounted for, but we seek general trends causing the largest differences between SNe 2011fe and 2017erp. Similar to Foley & Kirshner (2013) we have compared two well-observed examples, but larger samples (Smitka 2016; Pan et al. 2018) of SNe Ia might help disentangle multiple effects.

There is a connection between our proposed cause of the NUV-blue/red dispersion and the general trend seen by Thomas et al. (2011) and Milne et al. (2013) that the NUV-blue SNe Ia frequently have detections of C II in their spectra while NUV-red SNe Ia generally do not. Heringer et al. (2017) found that emission from iron can hide the absorption from carbon, implying that SNe Ia with carbon signatures have a lower metal content in their outer layers. As described above, SN 2017erp would be another exception to this general trend (as was SN 2005cf; Silverman et al. 2012), as there are dips in the early optical spectra redward of Si II 6355 Å that are most likely C II. However, the presence of C II and its detectability is not a binary property, and Parrent et al. (2011) discussed a variety of causes (such as S/N, abundance, and velocity differences), which may affect if, and at what epochs, C II is detectable. If metallicity is related to both the NUV dispersion and the strength of C II features, each would be expected to have a continuous distribution. A larger sample of SNe Ia with measurements of UV color and the strengths of C II (corrected to some common epoch or otherwise accounting for the time-variation of the C II strength) is needed to understand this further, treating both parameters as continuous variables.

Foley & Kirshner (2013) and Graham et al. (2015a) conjecture that metallicity is the cause of the mid-UV flux differences of the otherwise nearly identical SNe 2011fe and 2011by based on comparisons with models from Lentz et al. (2000). Multiple theoretical models also show near-UV differences (Höflich et al. 1998; Sauer et al. 2008; Walker et al. 2012; Wang et al. 2012; Baron et al. 2015; Miles et al. 2016), including the near-peak and later models of Lentz et al. (2000). The similarity of the SN 2017erp spectra in the near-UV region to the higher metallicity models of Walker et al. (2012) strengthen our confidence that at least some of the differences in the near-UV are caused by metallicity. The differences between the models, however, and the other factors affecting the UV make us cautious about quantitative statements regarding metallicity using the models. Further work is needed to resolve to what extent the differences between SNe 2011fe and 2011by and between SNe 2011fe and 2017erp are due to metallicity and how much is due to other causes. What we do think is clear, however, is that there are multiple regimes of UV dispersion—SNe Ia with similar optical colors and light-curve shapes can have different near-UV spectra, as shown here, as well as different near-UV photometric colors (Milne et al. 2013; Brown et al. 2017), and SNe Ia with similar optical and near-UV colors and light-curve shapes can have different mid-UV flux (Foley & Kirshner 2013; Graham et al. 2015b).

Foley et al. (2018) further tie the metallicity differences they infer between SNe 2011fe and 2011by to the significant luminosity differences between them without affecting the optical colors or spectra. Recent modeling by Miles et al. (2016) predicts that a change in progenitor metallicity does cause a change in the bolometric luminosity in the same direction as predicted by Timmes et al. (2003) and assumed by Foley et al. (2018). The models also, however, predict a change in the $\Delta m_{15}(B)$ of up to 0.4 mag, depending on the model, and changes in the temperature and thus spectral shape as well as numerous features in the UV and the optical. This makes it difficult to isolate an effect like metallicity.

In scientific experiments, one changes a single physical characteristic at a time (the independent variable) and measures the difference (if any) on one or more other characteristics (dependent variables). In an observational science, we have a multitude of observables that may or may not be dependent on each other. We may attempt to limit the number of differences by using subsamples where one observable is similar. In this case we compare SNe Ia with similar velocities and $\Delta m_{15}(B)$ and seek the cause of a difference in the UV flux continuum and features. However, if the cause of the UV flux differences also causes differences in other observables such as intrinsic $B-V$ color, velocity, or $\Delta m_{15}(B)$, then such sample cuts may hide the relevant correlations.

The multiplicity of models predicting different UV effects from metallicity (Höflich et al. 1998; Lentz et al. 2000; Sauer et al. 2008; Walker et al. 2012; Miles et al. 2016) as well as the other effects that could be going on (asymmetry, density gradients, etc., see, e.g., Brown et al. 2014b) make it seem premature to conclude metallicity is the only cause of either the near-UV or mid-UV differences at this time. Multiple physical differences likely exist between SNe 2011fe and 2017erp, which are not matched by the change of a single parameter like metallicity. What is needed are models that accurately predict the observed UV-optical-NIR spectra and light curves for a subset of SNe and grids of parameter variations. The large sample of UV, optical, and NIR spectra that now exist should be able to constrain the physical parameters that serve as inputs to the models.

5. Summary

We have presented the first *HST* UV spectra of a normal, NUV-red SN Ia 2017erp. These spectra allow us to predict the effect of reddening on the UV photometry for similar objects and show that SN 2017erp has redder UV-optical colors when reddening-corrected to similar optical colors. We find spectroscopic differences in the near-UV associated with the Ca H&K feature and the continuum near 2800–3300 Å. We show that the latter feature is strongly affected by changes in metallicity in the models by Walker et al. (2012), but further modeling work is necessary to allow the disentangling of likely multiple effects. Differences in the reddening inferred from different light-curve fitters and filter combinations, in addition to the different intrinsic colors of SN Ia models with varying metallicity, point to improvements needed to increase the accuracy of using SNe Ia as standard candles for distance measurements. Additionally we find that spectral differences between SN 2017erp and SN 2011fe are consistent with the SALT2 color law, implying that the law could be dominated by intrinsic differences, not dust, in the UV. Understanding the UV better is important for using SNe Ia as standard candles in the distant universe where the UV is redshifted into the observed bands and evolution in the progenitor properties might result in differences in the observables used for cosmology.

Support for program #14665 was provided by NASA through a grant from the Space Telescope Science Institute, which is operated by the Association of Universities for Research in Astronomy, Inc., under NASA contract NAS 5-26555. The *Swift* Optical/Ultraviolet Supernova Archive (SOUSA) is supported by NASA's Astrophysics Data Analysis Program through grant NNX13AF35G. We thank N. Suntzeff and K. Krisciunas for helpful comments and support during the process of analysis and writing. We acknowledge the work of Jamison Burke, Shuhrat A. Ehgamberdiev, Han Lin, Jun Mo, Liming Rui, and Lingzhi Wang in obtaining some of this data. This work made use of public data in the *Swift* data archive and the NASA/IPAC Extragalactic Database (NED), which is operated by the Jet Propulsion Laboratory, California Institute of Technology, under contract with NASA. This work makes use of observations from the Las Cumbres Observatory network and the Global Supernova Project. D.A.H., C.M., and G.H. are supported by NSF grant AST 1313484. Research by D.J.S. is supported by NSF grants AST-1821967, 1821987, 1813708, and 1813466. Based on observations obtained at the Gemini Observatory under programs GS-2017A-Q-33 (PI: Sand). Gemini is operated by the Association of Universities for Research in Astronomy, Inc., under a cooperative agreement with the NSF on behalf of the Gemini partnership: the NSF (United States), the National Research Council (Canada), CONICYT (Chile), Ministerio de Ciencia, Tecnología e Innovación Productiva (Argentina), and Ministério da Ciência, Tecnologia e Inovação (Brazil). The data were processed using the Gemini IRAF package. We thank the queue service observers and technical support staff at Gemini Observatory for their assistance. Some of the observations reported in this paper were obtained with the Southern African Large Telescope (SALT). This supernova research at Rutgers University is supported by NASA grant NNG17PX03C and US Department of Energy award DE-SC0011636. A.J.R. has been supported by the Australian Research Council through grant numbers CE110001020 and FT170100243. Syed A Uddin was supported by the Chinese Academy of Sciences President's International Fellowship Initiative grant No. 2016PM014. E.Y. H. acknowledges the support provided by the National Science Foundation under grant No. AST-1613472.

Facilities: HST(STIS), *Swift*(UVOT), Las Cumbres Observatory, Gemini South (GMOS, Flamingos-2), SALT (RSS), ANU(WiFeS).

Software: IRAF, PyRAF, PySALT.

ORCID iDs

Peter J. Brown https://orcid.org/0000-0001-6272-5507
Griffin Hosseinzadeh https://orcid.org/0000-0002-0832-2974
Saurabh W. Jha https://orcid.org/0000-0001-8738-6011
David Sand https://orcid.org/0000-0003-4102-380X
Xiaofeng Wang https://orcid.org/0000-0002-7334-2357
Iair Arcavi https://orcid.org/0000-0001-7090-4898
Chris R. Burns https://orcid.org/0000-0003-4625-6629
Tiara Diamond https://orcid.org/0000-0002-0805-1908
E. Y. Hsiao https://orcid.org/0000-0003-1039-2928
Curtis McCully https://orcid.org/0000-0001-5807-7893
Peter A. Milne https://orcid.org/0000-0002-0370-157X
Stefano Valenti https://orcid.org/0000-0001-8818-0795

References

Amanullah, R., Goobar, A., Johansson, J., et al. 2014, ApJL, 788, L21
Barbary, K., Barclay, T., Biswas, R., et al. 2016, SNCosmo: Python library for supernova cosmology, Astrophysics Source Code Library, ascl:1611.017
Baron, E., Hoeflich, P., Friesen, B., et al. 2015, MNRAS, 454, 2549
Betoule, M., Kessler, R., Guy, J., et al. 2014, A&A, 568, A22
Bravo, E., Domínguez, I., Badenes, C., Piersanti, L., & Straniero, O. 2010, ApJL, 711, L66
Breeveld, A. A., Landsman, W., Holland, S. T., et al. 2011, in AIP Conf. Proc. 1358, Gamma Ray Bursts 2010, ed. J. E. McEnery, J. L. Racusin, & N. Gehrels (Melville, NY: AIP), 373
Brown, P. J. 2014, ApJL, 796, L18
Brown, P. J., Baron, E., Milne, P., Roming, P. W. A., & Wang, L. 2015, ApJ, 809, 37
Brown, P. J., Breeveld, A. A., Holland, S., Kuin, P., & Pritchard, T. 2014a, A&SS, 354, 89
Brown, P. J., Kuin, P., Scalzo, R., et al. 2014b, ApJ, 787, 29
Brown, P. J., Landez, N. J., Milne, P. A., & Stritzinger, M. D. 2017, ApJ, 836, 232
Brown, P. J., Perry, J. M., Beeny, B. A., Milne, P. A., & Wang, X. 2018, ApJ, 867, 56
Brown, P. J., Roming, P. W. A., Milne, P., et al. 2010, ApJ, 721, 1608
Brown, T. M., Baliber, N., Bianco, F. B., et al. 2013, PASP, 125, 1031
Bufano, F., Immler, S., Turatto, M., et al. 2009, ApJ, 700, 1456

Burns, C. R., Stritzinger, M., Phillips, M. M., et al. 2011, AJ, 141, 19
Burns, C. R., Stritzinger, M., Phillips, M. M., et al. 2014, ApJ, 789, 32
Cardelli, J. A., Clayton, G. C., & Mathis, J. S. 1989, ApJ, 345, 245
Cinabro, D., Scolnic, D., Kessler, R., Li, A., & Miller, J. 2017, MNRAS, 466, 884
Cooke, J., Ellis, R. S., Sullivan, M., et al. 2011, ApJL, 727, L35
Crawford, S. M., Still, M., Schellart, P., et al. 2010, Proc. SPIE, 7737, 25
de Vaucouleurs, G., de Vaucouleurs, A., Corwin, H. G., Jr., et al. 1991, Third Reference Catalogue of Bright Galaxies. Vol. I, II, III (New York: Springer)
Eikenberry, S., Elston, R., Raines, S. N., et al. 2008, Proc. SPIE, 7014, 70140V
Ellis, R. S., Sullivan, M., Nugent, P. E., et al. 2008, ApJ, 674, 51
Foley, R. J. 2013, MNRAS, 435, 273
Foley, R. J., Filippenko, A. V., Aguilera, C., et al. 2008a, ApJ, 684, 68
Foley, R. J., Filippenko, A. V., & Jha, S. W. 2008b, ApJ, 686, 117
Foley, R. J., Filippenko, A. V., Kessler, R., et al. 2012a, AJ, 143, 113
Foley, R. J., Fox, O. D., McCully, C., et al. 2014, MNRAS, 443, 2887
Foley, R. J., Hoffmann, S. L., Macri, L. M., et al. 2018, arXiv:1806.08359
Foley, R. J., & Kirshner, R. P. 2013, ApJL, 769, L1
Foley, R. J., Kromer, M., Howie Marion, G., et al. 2012b, ApJL, 753, L5
Foley, R. J., Pan, Y.-C., Brown, P., et al. 2016, MNRAS, 461, 1308
Garavini, G., Nobili, S., Taubenberger, S., et al. 2007, A&A, 471, 527
Gehrels, N., Chincarini, G., Giommi, P., et al. 2004, ApJ, 611, 1005
Goldhaber, G., Groom, D. E., Kim, A., et al. 2001, ApJ, 558, 359
Goobar, A. 2008, ApJL, 686, L103
Graham, M. L., Foley, R. J., Zheng, W., et al. 2015a, MNRAS, 446, 2073
Graham, M. L., Valenti, S., Fulton, B. J., et al. 2015b, ApJ, 801, 136
Guy, J., Sullivan, M., Conley, A., et al. 2010, A&A, 523, A7
Hachinger, S., Mazzali, P. A., Sullivan, M., et al. 2013, MNRAS, 429, 2228
Heringer, E., van Kerkwijk, M. H., Sim, S. A., & Kerzendorf, W. E. 2017, ApJ, 846, 15
Höflich, P., Nomoto, K., Umeda, H., & Wheeler, J. C. 2000, ApJ, 528, 590
Höflich, P., Wheeler, J. C., & Thielemann, F. K. 1998, ApJ, 495, 617
Hsiao, E. Y., Burns, C. R., Contreras, C., et al. 2015, A&A, 578, A9
Hsiao, E. Y., Marion, G. H., Phillips, M. M., et al. 2013, ApJ, 766, 72
Huang, F., Li, J.-Z., Wang, X.-F., et al. 2012, RAA, 12, 1585
Itagaki, K. 2017, TNSTR, 647
Jha, S., Riess, A. G., & Kirshner, R. P. 2007, ApJ, 659, 122
Jha, S. W., Camacho, Y., Dettman, K., et al. 2017, ATel, 10490
Kasen, D., & Plewa, T. 2007, ApJ, 662, 459
Kessler, R., Becker, A. C., Cinabro, D., et al. 2009, ApJS, 185, 32
Kromer, M., & Sim, S. A. 2009, MNRAS, 398, 1809
Lentz, E. J., Baron, E., Branch, D., Hauschildt, P. H., & Nugent, P. E. 2000, ApJ, 530, 966
Maeda, K., Röpke, F. K., Fink, M., et al. 2010, ApJ, 712, 624
Maguire, K., Sullivan, M., Ellis, R. S., et al. 2012, MNRAS, 426, 2359
Marion, G. H., Vinko, J., Wheeler, J. C., et al. 2013, ApJ, 777, 40
Maund, J. R., Höflich, P., Patat, F., et al. 2010, ApJL, 725, L167
Mazzali, P. A., & Podsiadlowski, P. 2006, MNRAS, 369, L19
Mazzali, P. A., Sullivan, M., Hachinger, S., et al. 2014, MNRAS, 439, 1959
Miles, B. J., van Rossum, D. R., Townsley, D. M., et al. 2016, ApJ, 824, 59
Milne, P. A., Brown, P. J., Roming, P. W. A., Bufano, F., & Gehrels, N. 2013, ApJ, 779, 23
Milne, P. A., Foley, R. J., Brown, P. J., & Narayan, G. 2015, ApJ, 803, 20
Moreno-Raya, M. E., Mollá, M., López-Sánchez, Á. R., et al. 2016, ApJL, 818, L19
Pan, Y.-C., Foley, R. J., Filippenko, A. V., & Kuin, N. P. M. 2018, MNRAS, 479, 517
Pan, Y.-C., Foley, R. J., Kromer, M., et al. 2015, MNRAS, 452, 4307
Parrent, J. T., Thomas, R. C., Fesen, R. A., et al. 2011, ApJ, 732, 30
Pastorello, A., Taubenberger, S., Elias-Rosa, N., et al. 2007, MNRAS, 376, 1301
Pereira, R., Thomas, R. C., Aldering, G., et al. 2013, A&A, 554, A27
Perlmutter, S., Aldering, G., Goldhaber, G., et al. 1999, ApJ, 517, 565
Phillips, M. M. 1993, ApJL, 413, L105
Phillips, M. M., Lira, P., Suntzeff, N. B., et al. 1999, AJ, 118, 1766
Phillips, M. M., Simon, J. D., Morrell, N., et al. 2013, ApJ, 779, 38
Podsiadlowski, P., Mazzali, P. A., Lesaffre, P., Wolf, C., & Forster, F. 2006, arXiv:astro-ph/0608324
Poznanski, D., Ganeshalingam, M., Silverman, J. M., & Filippenko, A. V. 2011, MNRAS, 415, L81
Prevot, M. L., Lequeux, J., Prevot, L., Maurice, E., & Rocca-Volmerange, B. 1984, A&A, 132, 389
Prieto, J. L., Rest, A., & Suntzeff, N. B. 2006, ApJ, 647, 501
Riess, A. G., Filippenko, A. V., Challis, P., et al. 1998, AJ, 116, 1009
Riess, A. G., Macri, L. M., Hoffmann, S. L., et al. 2016, ApJ, 826, 56
Riess, A. G., Press, W. H., & Kirshner, R. P. 1996, ApJ, 473, 88
Riess, A. G., Strolger, L.-G., Tonry, J., et al. 2004, ApJ, 607, 665
Roming, P. W. A., Kennedy, T. E., Mason, K. O., et al. 2005, SSRv, 120, 95
Sauer, D. N., Mazzali, P. A., Blondin, S., et al. 2008, MNRAS, 391, 1605
Schlafly, E. F., & Finkbeiner, D. P. 2011, ApJ, 737, 103
Schlegel, D. J., Finkbeiner, D. P., & Davis, M. 1998, ApJ, 500, 525
Scolnic, D. M., Jones, D. O., Rest, A., et al. 2018, ApJ, 859, 101
Scolnic, D. M., Riess, A. G., Foley, R. J., et al. 2014, ApJ, 780, 37
Silverman, J. M., & Filippenko, A. V. 2012, MNRAS, 425, 1917
Silverman, J. M., Kong, J. J., & Filippenko, A. V. 2012, MNRAS, 425, 1819
Smith, M. P., Nordsieck, K. H., Burgh, E. B., et al. 2006, Proc. SPIE, 6269, 62692A
Smitka, M. T. 2016, PhD thesis, Texas A&M Univ.
Theureau, G., Coudreau, N., Hallet, N., et al. 2005, A&A, 430, 373
Thomas, R. C., Aldering, G., Antilogus, P., et al. 2011, ApJ, 743, 27
Timmes, F. X., Brown, E. F., & Truran, J. W. 2003, ApJL, 590, L83
Tripp, R. 1998, A&A, 331, 815
Tripp, R., & Branch, D. 1999, ApJ, 525, 209
Vacca, W. D., Cushing, M. C., & Rayner, J. T. 2003, PASP, 115, 389
Valenti, S., Howell, D. A., Stritzinger, M. D., et al. 2016, MNRAS, 459, 3939
Vinkó, J., Ordasi, A., Szalai, T., et al. 2018, PASP, 130, 064101
Vinkó, J., Sárneczky, K., Takáts, K., et al. 2012, A&A, 546, A12
Walker, E. S., Hachinger, S., Mazzali, P. A., et al. 2012, MNRAS, 427, 103
Wang, X., Filippenko, A. V., Ganeshalingam, M., et al. 2009a, ApJL, 699, L139
Wang, X., Li, W., Filippenko, A. V., et al. 2009b, ApJ, 697, 380
Wang, X., Wang, L., Filippenko, A. V., et al. 2012, ApJ, 749, 126
Wang, X., Wang, L., Zhou, X., Lou, Y.-Q., & Li, Z. 2005, ApJL, 620, L87
Zhang, K., Wang, X., Zhang, J., et al. 2016, ApJ, 820, 67